

Thermodynamic Structure of the Solar Corona: Tomographic Reconstructions and MHD Modeling

Diego G. Lloveras¹  · Alberto
M. Vásquez^{1,2}  · Federico A. Nuevo^{1,3}  ·
Cecilia Mac Cormack^{1,2}  ·
Nishtha Sachdeva⁴  · Ward Manchester
IV⁴  · Bartholomeus Van der Holst⁴  ·
Richard A. Frazin⁴ 

© Springer

Abstract Observational techniques play an essential role in advancing our understanding of the physical processes governing the solar corona, providing

✉ D.G. Lloveras
dlloveras@iafe.uba.ar
A.M. Vásquez
albert@iafe.uba.ar
F.A. Nuevo
federico@iafe.uba.ar
C. Mac Cormack
cmaccormack@iafe.uba.ar
N. Sachdeva
nishthas@umich.edu
W. Manchester IV
chipm@umich.edu
B. Van der Holst
bartvand@umich.edu
R.A. Frazin
rfrazin@umich.edu

- ¹ Instituto de Astronomía y Física del Espacio (IAFE), CONICET-UBA, CC 67 - Suc 28, (C1428ZAA) Ciudad Autónoma de Buenos Aires, Argentina
- ² Universidad Nacional de Tres de Febrero (UNTREF). Departamento de Ciencia y Tecnología, Sáenz Peña, Argentina.
- ³ Ciclo Básico Común (CBC), Universidad de Buenos Aires (UBA), Buenos Aires, Argentina
- ⁴ Department of Climate and Space Sciences and Engineering (CLaSP), University of Michigan, 2455 Hayward Street, Ann Arbor, MI 48109-2143, USA

in particular validation data for three-dimensional (3D) magnetohydrodynamic (MHD) models of the solar atmosphere. Solar rotational tomography is currently the sole observational technique able to provide a 3D quantitative description of the solar corona at a global scale. Based on extreme ultraviolet images of space borne instruments, differential emission measure tomography (DEMT) allows constructing 3D maps of the coronal electron density and temperature at heliocentric heights below $\approx 1.25 R_{\odot}$. We carry out a study of the corona through DEMT reconstructions and MHD simulations, using the latest version of the Alfvén Wave Solar Model (AWSoM) developed at the University of Michigan as a component of the Space Weather Modeling Framework. Two target rotations were selected from the solar minimum between solar cycles (SC) 23 and 24 and the end of the declining phase of SC 24. The 3D DEMT and MHD models are analysed and compared in distinct coronal magnetic structures. We report in quantitative detail on the 3D thermodynamic structure of the inner corona as revealed by the DEMT analysis. We show the existence of diverse types of temperature structures in the low and mid latitudes of the streamer belt. We estimate the heating energy required to keep them stable, which we argue may be accounted for by Alfvén waves. We also show that results of the latest version of the AWSoM model overall agree with DEMT reconstructions within a $\approx 20\%$ accuracy. We highlight some details of the AWSoM model that should be improved to better reproduce tomographic results, in particular concerning the source region of the fast and slow components of the solar wind.

Keywords: Solar Cycle, Observations; Corona,E; Corona, Structures

1. Introduction

Being the region where the solar atmosphere is heated, the solar wind accelerated, and where impulsive events such as solar flares and coronal mass ejections are energized, observing and modeling of the solar corona are of great relevance to improving our understanding of the Sun-Earth environment. To advance our knowledge of the physics of the solar corona, as well as to enhance and validate three-dimensional (3D) models, information derived from observational data plays a key role. Solar rotational tomography (SRT) is currently the sole observational technique able to provide a quantitative empirical description of the 3D distribution of some fundamental plasma parameters of the solar corona at a global scale.

To study the 3D structure of the quiet-Sun global corona, SRT has proven to be a powerful tool. In SRT, solar rotation is taken advantage of, so that instruments gather time series of images covering all viewing angles of the solar corona. This allows posing an inversion problem to solve for the unknown 3D distribution of specific quantities of the solar corona. Based on extreme ultraviolet EUV images, taken in several channels sensitive to different temperatures, differential emission measure tomography (DEMT) allows reconstruction of the 3D distribution of the differential emission measure (DEM). The final product of DEMT is in the form of 3D maps of electron density and temperature, covering

the range of heliocentric heights $\lesssim 1.25 R_{\odot}$. The technique was first developed by Frazin, Vásquez, and Kamalabadi (2009), and first applied to the observational study of coronal structures by Vásquez, Frazin, and Kamalabadi (2009). A recent review on DENT was published by Vásquez (2016). The technique is summarized in Section 2.1.

The combination of DENT with global magnetic models provides insight into the 3D thermodynamical structure of the global quiet-Sun corona. DENT was first combined with a potential field source surface (PFSS) model by Huang *et al.* (2012) and Nuevo *et al.* (2013). More recently, Lloveras *et al.* (2017) combined DENT with PFSS models to study the thermodynamics of the global solar corona in specific magnetic structures for two target rotations selected from the last two solar minimum epochs. Also combining DENT with a PFSS model, Mac Cormack *et al.* (2017) developed a new DENT product that estimates the energy input flux required at the coronal base in order to maintain stable coronal loops. In this article, DENT is first combined with the magnetic field of a magnetohydrodynamic (MHD) model.

The Alfvén Wave Solar atmosphere Model (AWSoM) within the Space Weather Modeling Framework (SWMF) is a three-dimensional (3D) physics-based, data-driven MHD model extending from the upper chromosphere, to the upper corona and to 1 AU and beyond (van der Holst *et al.*, 2010, 2014). The single data input of the model is a magnetogram of the global corona, used as boundary condition for the simulation. As new improvements are implemented, the model is continuously being validated with observations. DENT results were used by Jin *et al.* (2012) and Oran *et al.* (2015) to validate AWSoM results finding an agreement within 50% in density and electron temperature in the low corona. More recently, Sachdeva *et al.* (2019) compared the results of the latest version of AWSoM model with DENT products in a globally fashion, obtaining an agreement within 20%.

In this work, the AWSoM model is used with two purposes. Firstly, to provide an MHD model of the coronal magnetic field to be used to study the DENT results along magnetic field lines. Secondly, to provide thermodynamic results to be compared with those reconstructed by DENT.

Combining the DENT and AWSoM models, we carry out a detailed quantitative analysis of two target rotations. We selected Carrington rotation (CR)-2082 (2009, 05 April through 03 May) during the Solar Cycle (SC) 23/24 minimum, and CR-2208 (2018, 02 September through 29 September) during the end of the declining phase of SC 24. In the case of CR-2082, the DENT analysis is based on data taken by the *Extreme UltraViolet Imager Behind* (EUVI-B: Wuelser *et al.* 2004) on board the *Solar TERrestrial RELations Observatory* (STEREO), while the AWSoM model uses the synoptic magnetogram provided by the Global Oscillation Network Group (GONG). In the case of CR-2208, the DENT analysis is based in data taken by the *Atmospheric Imaging Assembly instrument* (AIA: Lemen *et al.* 2012) on board the *Solar Dynamics Observatory* (SDO), while the AWSoM model uses the magnetogram provide by the Air Force Data Assimilation Photospheric flux Transport (ADAPT)-GONG model.

Section 2.1 and 2.2 summarize the DENT technique and the AWSoM model, respectively. Section 2.3 details the method used to trace the DENT results

along the field lines of the magnetic model. Section 2.4 details the method that allows determination of the energy input flux at the coronal base. In Section 3.1 the quantitative detailed DENT analysis of both target rotations is shown, and in Section 3.2 the AWSOM and DENT results are compared. Finally, Section 4 summarizes and discusses the main conclusions of this analysis, and anticipates further planned work.

2. Methodology

2.1. DENT Reconstructions

As detailed in Section 1, target rotations CR-2082 and CR-2208 were selected to carry out DENT reconstructions, based on data taken by the STEREO/EUVI-B and SDO/AIA instruments, respectively. The EUVI and AIA data were prepared using the latest processing tools and calibration corrections provided by their teams through the SolarSoft package. For this work, we introduced two improvements in the implementation of the DENT technique, as described next.

While in all previous DENT studies full-disk data was used to perform tomography, in this work we opt to only use off-limb data. In this way, the smallest scale and brighter coronal features seen on disk (most typically in the 171 Å band) are not included. This has two implications. Firstly, the fast dynamics that typically characterizes those structures is absent from the data. Secondly, only half synodic rotation worth of data is needed to constrain the inversion problem for the whole coronal volume. As a result, artifacts induced by coronal dynamics are reduced compared to previous DENT reconstructions.

The solution of the tomographic problem involves inversion of a very large sparse matrix. Such inversion problems are characterized by spurious high-frequency artifacts in the solution, which can be mitigated through regularization techniques (Frazin, 2000). In the case of DENT, all previous efforts used the 2D scheme implemented by Frazin, Vásquez, and Kamalabadi (2009), using a finite difference matrix operator to approximate angular derivatives in both latitude and longitude. Also new to the present work, is the implementation of an expanded 3D regularization scheme, which adds to the previous scheme a finite difference matrix operator to approximate radial derivatives. In this way, the tomographic inversion problem is performed penalizing nonphysical high-frequency artifacts in all three spatial directions. As a result, tomographic reconstructions behave more smoothly close to the radial boundaries of the computational grid when compared to previous reconstructions.

In DENT, the inner corona in the range of heliocentric heights $\lesssim 1.25 R_{\odot}$ is discretized in a spherical computational grid. The size of the tomographic grid cell (or voxel) is typically set to $0.01 R_{\odot}$ in the radial direction and 2° in both the latitudinal and longitudinal directions. The cadence of the data time-series is set to 6 hr. The main product of the technique is the local DEM (LDEM) at each voxel, a measure of the temperature distribution of the plasma contained in it. We summarize next the main aspects of DENT required for the analysis of this work.

In a first step, the time series of EUV images is used to solve a solar SRT problem, for each EUV band independently. As a result, the 3D distribution of the so called *filter band emissivity* (FBE) is determined for each band separately. The FBE, an emissivity-type quantity, is defined as the wavelength integral of the coronal EUV spectral emissivity and the telescope's passband function of each EUV channel. Line-of-sight (LOS) integration of the FBE provides synthetic images that can be quantitatively compared to the real data in the time series. To find the FBE, the tomographic problem is posed as a global optimization problem in which the quadratic norm of the difference between all pairs of synthetic and real images is minimized.

Due to unresolved coronal dynamics, tomographic reconstructions exhibit negative values of the reconstructed FBE, or zero when the solution is constrained to positive values (Frazin, 2000; Frazin, Vásquez, and Kamalabadi, 2009). These non-reconstructed voxels are indicated in black color in the latitude-longitude (Carrington) maps of DENT results in Section 3.

In a second step, the FBE values obtained for all bands in each voxel of the tomographic grid are used to constrain the determination of the local-DEM (LDEM) which, as described in Section 1, describes the temperature distribution of the plasma within the individual voxel. Specifically, at each tomographic voxel i , the FBE of the band k is related to the LDEM of the voxel according to

$$\text{FBE}_i^{(k)} = \int dT \text{LDEM}_i(T) \text{TRF}^{(k)}(T), \quad k = 1, \dots, K \quad (1)$$

where K is the number EUV bands, and $\text{TRF}^{(k)}$ is the *temperature response function* of the k -th detector. In this work, the TRFs are computed based on the (known) channel's passband times the coronal emissivity at that temperature (normalized by the squared electron density). The emissivity model used here is provided by the latest version of the CHIANTI atomic database and plasma emission model (Del Zanna *et al.*, 2015; Landi *et al.*, 2013).

In this work, data from three EUV bands was used: 171, 193 and 211 Å in the case of AIA, and 171, 195 and 284 Å bands in the case of EUVI. When using data from three bands, a Gaussian model for the LDEM is able to accurately predict the FBEs (Nuevo *et al.*, 2015). In each tomographic voxel, the problem is then reduced to finding the values of the three free parameters of the Gaussian (centroid, standard deviation, and area) that best reproduce the three tomographically reconstructed values of FBE in that voxel.

Once the LDEM is determined at each voxel, the LDEM-averaged squared electron density N_m^2 and electron temperature T_m in the voxel can be computed by taking its zeroth and first moments over temperature. More specifically, at the i -th voxel,

$$N_{m,i}^2 = \langle N_e^2 \rangle_i = \int dT \text{LDEM}_i(T), \quad (2)$$

$$T_{m,i} = \langle T_e \rangle_i = \frac{1}{\langle N_e^2 \rangle_i} \int dT T \text{LDEM}_i(T). \quad (3)$$

Next, we define a measure of the accuracy of the LDEM model to predict the tomographic FBEs in each voxel, as

$$R_i \equiv (1/K) \sum_{k=1}^K \left| 1 - \text{FBE}_{i,\text{syn}}^{(k)} / \text{FBE}_{i,\text{tom}}^{(k)} \right|, \quad (4)$$

being the average relative difference between the tomographic and the synthetic FBEs. The final product of DEMA is in the form of 3D maps of the LDEM-averaged quantities $\sqrt{N_m^2}$ and T_m , as well as of the measure R . For a full description of the DEMA technique we refer the reader to Frazin, Vásquez, and Kamalabadi (2009).

2.2. AWSoM Simulations

AWSoM is a three-temperature, MHD model of the solar corona and inner heliosphere which provides the 3D distribution of density and temperatures as well as the 3D magnetic structure and velocity of the solar wind. In this work, we use AWSoM model simulated results below $1.25 R_\odot$ to correspond to the DEMA analysis region.

Heating of the solar corona is addressed by including the non-linear interaction of forward and counter-propagating (reflected) Alfvén waves which results in a turbulent cascade. This dissipated turbulent energy is distributed over anisotropic (parallel and perpendicular) proton temperatures and isotropic electron temperature using theories of linear wave damping and stochastic heating.

The model accounts for both collisional and collision-less electron heat conduction and does not use ad-hoc heating functions. The extended MHD equations including radiative cooling, heat conduction and wave turbulence within AWSoM (van der Holst *et al.*, 2014) are solved using the Block-Adaptive-Tree-Solarwind-Roe-Upwind Scheme (BATS-R-US, Powell *et al.*, 1999; Tóth *et al.*, 2012) numerical scheme.

In a previous version of the model, the cascade time of the major wave was used to determine the wave damping rate (Chandran *et al.*, 2011; van der Holst *et al.*, 2014). In its present version, the energy partitioning improved by using the Alfvén wave number associated with the damping rate as determined by the critical balance condition, which uses the cascade time of the minor wave (Lithwick, Goldreich, and Sridhar, 2007). This leads to more electron heating and less solar wind acceleration (van der Holst, 2019).

The inner boundary of AWSoM is located at the base of the transition region (at $\approx 1.0 R_\odot$). In reality, the thin transition region (TR) has steep gradients in temperature and density as a result of the balance between coronal heating, heat conduction and the radiative losses. To resolve these gradients in a global model would require excessive numerical resources. As described in Lionello, Linker, and Mikić (2009) and Sokolov *et al.* (2013), the TR is artificially broadened to be resolved with a finest grid resolution of $0.001 R_\odot$. To ensure that the base of the TR is not affected by chromospheric evaporation we overestimate the density at the inner boundary, $N_e = N_i = N_\odot = 2 \times 10^{17} \text{ m}^{-3}$ corresponding to the isotropic temperature values, $T_e = T_i = T_{i\parallel} = T_\odot = 50,000 \text{ K}$. The upper chromosphere

is required to extend radially for the density to fall rapidly to correct (lower) values (Lionello, Linker, and Mikić, 2009). At this level, the radiative losses are sufficiently low so that the temperature can increase monotonically with height and form the transition region. Since the broadening of the transition region pushes the corona outwards, the AWSoM model achieves coronal conditions at height $\approx 1.05 R_{\odot}$, below which results can not then be compared to coronal tomographic reconstructions.

To drive the AWSoM model, estimates of the photospheric magnetic field of the Sun are the main input. Synoptic magnetograms are used to specify the initial and the boundary conditions of the magnetic field. We use the PFSS model to extrapolate the 3D magnetic field (from the 2D photospheric magnetic field maps) using spherical harmonics. The source surface is taken to be at $2.5 R_{\odot}$. The Global Oscillation Network Group (GONG) provides synoptic full-disk surface maps of the radial magnetic field component of the Sun. However, since the polar regions are not well observed from the ecliptic, GONG estimates the polar fields by fitting a polynomial to neighboring observed latitudes, which might lead to inaccuracies. An improvement over these maps is provided by the Air Force Data Assimilation Photospheric Flux Transport (ADAPT) model (Worden and Harvey, 2000), which creates synchronic-synoptic maps by incorporating supergranulation, meridional circulation, and differential rotation. These maps provide a physics-based description of the unobserved polar magnetic fields (Arge *et al.*, 2010; Henney *et al.*, 2012). In this work, we use the GONG synoptic map as input for CR-2082 (ADAPT-GONG maps are unavailable for CR-2082) and the ADAPT-GONG global magnetic field map for CR-2208. Based on results from previous efforts, for CR-2082 the magnetic field from the GONG map is scaled up by a factor of 1.85 for weak fields ($B_r < 5$ G), while no modification is applied in the case of the ADAPT-GONG map for CR-2208. The AWSoM steady-state simulation set-up and input parameters for both rotations are described below.

To account for the energy partitioning between electrons and protons, based on Chandran *et al.* (2011), we set the stochastic heating exponent equal to 0.21 and the amplitude equal to 0.18, for both rotations. The boundary condition for Alfvén wave energy is given by the poynting flux (S_A) of the outgoing wave, $(S_A/B)_{\odot} = 1.1 \times 10^6 \text{ W m}^{-2} \text{ T}^{-1}$ and $1.0 \times 10^6 \text{ W m}^{-2} \text{ T}^{-1}$ for CR-2082 and CR-2208, respectively, with B_{\odot} being the field strength at the inner boundary. The correlation length of the Alfvén waves is set to, $L_{\perp} \sqrt{B} = 1.5 \times 10^5 \text{ m} \sqrt{T}$.

The computational domain of the solar corona extends from 1 to $24 R_{\odot}$. The spherical grid in the solar corona is radially stretched (with a maximum resolution of $0.001 R_{\odot}$ near the Sun) with the z-axis aligned with the rotation axis in Heliographic Rotation coordinates. The Adaptive Mesh Refinement (AMR) resolves the angular cell size to 1.4° in the range of heights $1 - 1.7 R_{\odot}$ and beyond $2.8 R_{\odot}$. **NOTE: (by Albert) does this make sense?** The solar corona component uses about 3 million cells on a $6 \times 8 \times 8$ grid blocks (for CR-2208) and $6 \times 4 \times 4$ grid blocks for CR-2082. Local time stepping is used to speed up the steady state convergence. The AWSoM simulation results of the structure of the solar corona for solar minimum conditions represented by CR-2082 and CR-2208 are compared to the DENT as described in the results section.

2.3. Tracing Results Along Magnetic Field lines

To determine the electron density and temperature along individual magnetic field lines, first both the thermodynamic results and the magnetic field obtained with the AWSoM model were interpolated into the DENT grid. Then, the geometry of the field lines is determined by numerical integration of the first order differential equations $dr/B_r = r d\theta/B_\theta = r \sin(\theta) d\phi/B_\phi$, both inwards and outwards, from the specified 3D coordinates of a starting point. In order to evenly sample the whole volume spanned by the DENT reconstructions, one starting point is selected at the center of each tomographic cell at 6 uniformly spaced heights, ranging from 1.025 to $1.225 R_\odot$, and every 2° in both latitude and longitude, for a total of 97,200 starting points.

For analysis purposes, the traced magnetic field lines are classified as open or closed according to their full geometry. Each closed field line is further classified as “small” or “large”, according to its coronal length L being respectively smaller or larger than the median value of the whole population, which is $\text{Md}(L) \approx 0.5 R_\odot$ for both rotations. Finally, each closed magnetic field line is separated in its two “legs”, defined as the two segments that go from each of its two footpoints (*i.e.* their location at $r = 1 R_\odot$) to its apex (*i.e.*, the location of maximum height).

At this stage, DENT and AWSoM products can be traced along open and closed magnetic field lines. Once the field line geometry is computed in high spatial resolution, only one sample point per tomographic cell is kept (the median one). As a result, for each field line one data point per tomographic cell is obtained. This approach was firstly used by Huang *et al.* (2012) to study temperature structures in the solar minimum corona and by Nuevo *et al.* (2013) to expand that analysis to rotations with different level of activity.

For each open field line and for each closed field leg, an exponential fit was applied to the electron density data points and a linear fit applied to the electron temperature data points. For the DENT model the data points used were $\sqrt{N_m^2(r)}$ and $T_m(r)$, and in case of the AWSoM models the data points used were $N_e(r)$ and $T_e(r)$. The exponential and linear fit equations are described by

$$\sqrt{N_m^2} = N_0 \exp[-(h/\lambda_N) / (r/R_\odot)] \quad (5)$$

$$T_m = T_0 + m h \quad (6)$$

where $h \equiv r - 1 R_\odot$ is the coronal height measured from the photosphere. In the electron density fit, $\lambda_N [R_\odot]$ is the density scale height and $N_0 [\text{cm}^{-3}]$ is the electron density at the footpoint ($h = 0$) of the loop. In the electron temperature fit, $m [\text{MK}/R_\odot]$ is the slope and $T_0 [\text{MK}]$ is the electron temperature at the footpoint of the loop. The slope m estimates the radial gradient of the electron temperature along the loop, which we denote as $m = \nabla_r T_m$ hereafter, being $\nabla_r \equiv \mathbf{e}_r \cdot \nabla$ the radial derivative operator, where \mathbf{e}_r is the heliocentric radial unit vector.

In the case of the electron density, the fitted function corresponds to the isothermal hydrostatic equilibrium solution, allowing for variation of the solar

gravitational acceleration with height. This choice of function provides a straightforward means to directly evaluate how compatible is the observed coronal thermodynamical state with the hydrostatic solution.

Coronal magnetic structures for which temperature increases/decreases with height (in the inner corona) were dubbed as “up”/“down” loops by Huang *et al.* (2012) and Nuevo *et al.* (2013), who first reported their presence by means of DENT studies. As speculated by the authors of those works, loops of type down can be expected if the heating deposition is strongly confined near the coronal base of a magnetic loop. Down loops were first predicted by Serio *et al.* (1981), and later on by Aschwanden and Schrijver (2002). In a recent study, Schiff and Cranmer (2016) reproduced both down and up loops by means of numerical simulations, using a 1D steady-state model and considering time-averaged heating rates.

To determine if the leg of a traced field line is of type up or down, we first determine the Pearson correlation coefficient $\rho(T, r)$ between the DENT temperature T_m and the heliocentric height r data points. We then select field lines for which the temperature is significantly correlated with height by requiring $|\rho(T, r)| > 0.5$. To test the goodness of the fit to the temperature-height data we perform a chi-squared test (Press *et al.*, 2002) considering the uncertainty of the DENT data points, selecting legs for which the fit matches the data with a 90% confidence level. In this way, legs for which the DENT temperature does not show a significant correlation with height, or the linear fit to temperature is not good enough, are excluded from the analysis. The test is also applied to the density-height data points, to ensure the trend is reasonably represented by the exponential fit. Finally, selected legs are then classified as up or down according to if $\nabla_r T_m > 0$ or $\nabla_r T_m < 0$, respectively. The linear fit allows characterization of the variation of T_m with height by means of a characteristic temperature gradient $\nabla_r T_m$ [MK/R_⊙] along each leg. The chi-squared test to evaluate the quality of the fits considers the uncertainty level in the DENT products due to systematic sources (radiometric calibration and tomographic regularization), that Lloveras *et al.* (2017) estimated to be $\Delta T_m \approx 10\%$ and $\Delta \sqrt{N_m^2} \approx 5\%$. In summary, to be selected a leg must meet all three following conditions:

- i) The leg must go through at least five tomographic grid cells with reconstructed data, and there must be at least one data point in each third of the range of heights spanned by the leg. This requirement is set to ensure a reasonably spread sample of heights along the leg.
- ii) The DENT temperature and height data points must meet $|\rho(T, r)| > 0.5$.
- iii) The confidence level of both the exponential and linear fits must be larger than 90%.

To characterize the global thermodynamic state of the inner solar corona in distinct magnetic structures, the DENT and AWSOM results were traced along the magnetic field lines of the latter model. Based on the geometry and size of the loops, as well as on their thermodynamical properties, their legs were classified in four different types in this work:

- Type 0: closed-small-down with footpoints in the range $|\text{latitude}| < 50^\circ$.

- Type I: closed-small-up with footpoints in the range $|\text{latitude}| < 50^\circ$.
- Type II: closed-large-up with footpoints in the range $|\text{latitude}| > 40^\circ$.
- Type III: open with footpoint in the range $|\text{latitude}| > 60^\circ$.

Legs of type down turn out to have a significant population only for closed-small loops. In the case of closed-large loops and open field lines, there are very few cases of type down. Hence, the requirement of being up for legs of type II and III is included above to select the vastly dominating population in each case. In Section 3, the results of both the DENT and AWSOM models in the distinct magnetic structures are statistically analysed. As shown in Section 3.1, classification of legs from type 0 through II allows studying the streamer belt in three distinct, progressively outer layers.

2.4. Energy Input Flux

The high temperature of the corona requires heating mechanisms to compensate for the energy losses. While the vast majority of the existing literature on coronal heating focuses on active regions (ARs), some studies have been dedicated to the heating of quiet-Sun regions. In particular, Mac Cormack *et al.* (2017) developed a new application of the DENT technique to estimate the energy input flux required at the base of quiet-Sun coronal loops to maintain stability. The technique is based on tracing the DENT results along field lines of a global coronal magnetic model, just as described in Section 2.3.

Consider a static energy balance for each magnetic flux tube, in which the dominating losses of radiative power (E_r) and thermal conduction power (E_c) are compensated by a coronal heating power (E_h) (Aschwanden, 2004):

$$E_h(s) = E_r(s) + E_c(s), \quad (7)$$

where s is the position along the flux tube and the power quantities are in units of $[\text{erg sec}^{-1} \text{ cm}^{-3}]$.

The thermal conduction power E_c equals the divergence of the conductive heat flux F_c , *i.e.* $E_c(s) = [1/A(s)] d[A(s) F_c(s)]/ds$, where $A(s)$ is the transversal area of the magnetic flux tube at position s . Under a quiescent solar corona plasma regime, the conductive flux is assumed to be dominated by the electron thermal conduction, described by the usual Spitzer model (Spitzer, 1962)

$$F_c(s) = -\kappa_0 T(s)^{5/2} \frac{dT}{ds}(s), \quad (8)$$

where $\kappa_0 = 9.2 \times 10^{-7} \text{ erg sec}^{-1} \text{ K}^{-7/2}$ is the Spitzer thermal conductivity.

Radiative power depends on the amount of plasma in certain temperatures that can radiate.

In the corona, EUV emission is dominated by collisions of the emitting ions with free electrons, so that the radiative power scales as N_e^2 . The radiative power of an isothermal plasma at temperature T is then computed as $E_r = N_e^2 \Lambda(T)$, where the radiative loss function $\Lambda(T)$ is calculated by means of an emission

model. In this work we used the latest version of the atomic database and plasma emission model CHIANTI (Del Zanna *et al.*, 2015). The radiative power in terms of the LDEM is then given by:

$$E_r = \int dT \text{LDEM}(T) \Lambda(T). \quad (9)$$

The energy balance given by Equation 7 is then integrated in the volume of any given coronal magnetic flux tube. Dividing the result by the flux tube area at the coronal base, and making use of the soleidonal conditon of the magnetic field, a field line integrated version of that energy balance is found,

$$\phi_h = \phi_r + \phi_c, \quad (10)$$

where the line-integrated flux quantities $\phi_{r,c} [\text{erg sec}^{-1} \text{cm}^{-2}]$ are given by (Mac Cormack *et al.*, 2017),

$$\phi_r = \left(\frac{B_0 B_L}{B_0 + B_L} \right) \int_0^L ds \frac{E_r(s)}{B(s)}, \quad (11)$$

$$\phi_c = \left(\frac{B_0 F_{c,L} - B_L F_{c,0}}{B_0 + B_L} \right), \quad (12)$$

where L is the length of the loop, and B_0 and B_L are the values of the magnetic field at the footpoint locations of the loop in the coronal base, namely $s = 0$ and $s = L$. Note that, for any given field line, all quantities in these two expresions can be computed from the DMT results traced along field lines, and the AWSOM magnetic field model, through Equations 8-9. Once computed, the quantity ϕ_h can be calculated, which is the energy input flux required at the coronal base of each coronal field-line to mantain a stable coronal structure.

3. Results

3.1. Tomographic Results

As described in Section 2.1, we carried out DMT reconstructions of the coronal structure for target rotations CR-2082 and CR-2208 using STEREO/EUVI and SDO/AIA data, respectively. Once the LDEM was determined for each rotation, the square root of the mean value of the electron density squared ($\sqrt{N_m^2}$) and the electron mean temperature (T_m) were computed at each voxel of the tomographic computational grid by means of Equations 2 and 3, and the measure R was calculated by means of Equation 4.

As an example, Figures 1 and 2 show latitude-longitude maps of DMT results for both rotations. Three different heights of interest are selected from the tomographic grid, providing also a detailed 3D view of the tomographic results: the lowest height of the tomographic grid ($1.025 R_\odot$), the lowest height where

the AWSoM results are fully consistent with coronal conditions ($1.065 R_{\odot}$), and a middle height of the tomographic grid ($1.105 R_{\odot}$). Black voxels correspond to non-reconstructed voxels (see Section 2.1). Thick-black curves indicate the open/closed boundaries of the magnetic field of the AWSoM model, detailed in Section 2.2.

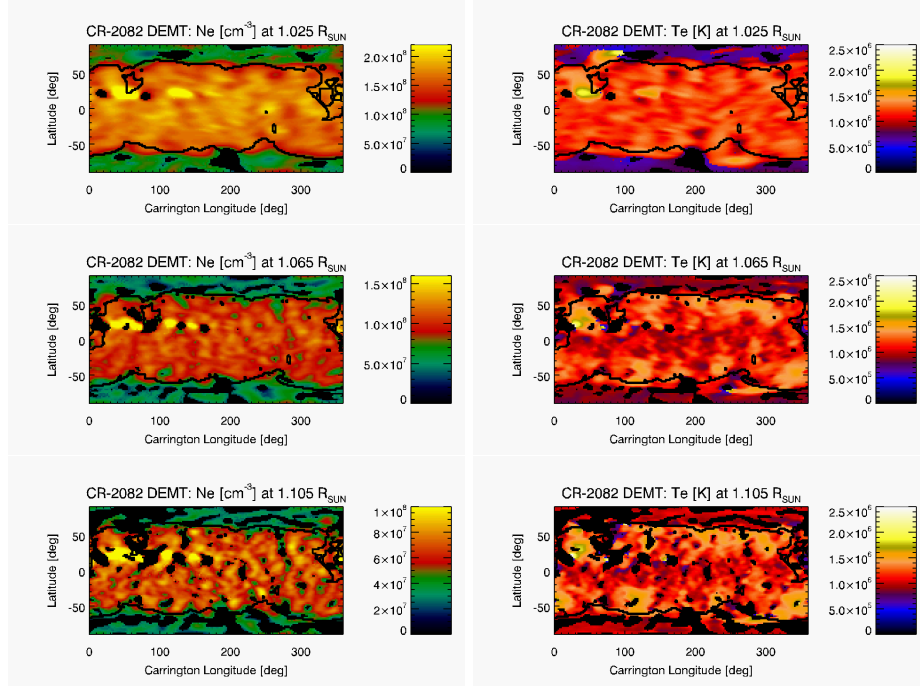


Figure 1. Carrington maps of DMT products $\sqrt{N_m^2}$ (left panels) and T_m (right panels) for CR-2082. Top, middle and bottom panels show the results at three heliocentric heights, 1.025, 1.065 and $1.105 R_{\odot}$ respectively. Black voxels correspond to non-reconstructed regions (see text in Section 3.1) and thick-black curves indicate the open/closed boundaries.

Both target rotations are highly axisymmetric, *i.e.* characterized by a high azimuthal symmetry. Rotation CR-2082 showed two small ARs, both near latitude $+30^\circ$ and around longitudes 50° and 120° (not identified in the NOAA catalog). Rotation CR-2208 showed two ARs, both near latitude $+5^\circ$ and around longitudes 140° and 300° (NOAA 12722, 12721).

The magnetically open and closed regions of the AWSoM model are associated with Coronal holes (CHs) and the equatorial streamer belt, respectively. The location of the open/closed boundaries derived from the respective AWSoM model quite accurately matches the regions of the DMT maps, which exhibit the strongest latitudinal gradient of both the electron density and temperature.

Figures 1 and 2 show that the DMT reconstruction of the streamer belt is characterized by relatively higher densities and temperatures in comparison to the CHs. They also show that the streamer belt region of CR-2082 was denser and colder than that of CR-2208. In the case of CR-2082, which belongs to the

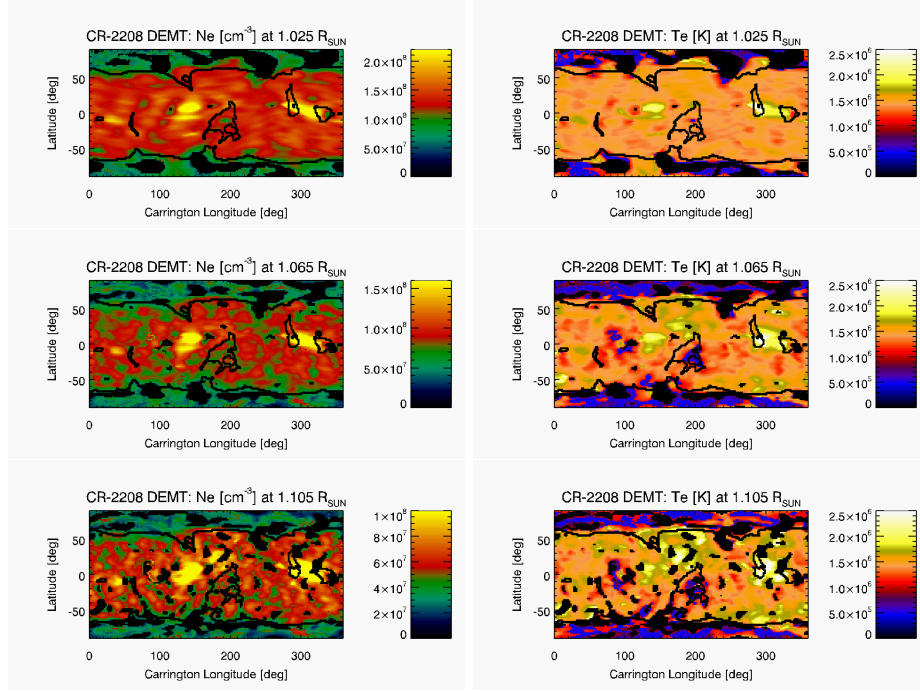


Figure 2. Same as Figure 1 but for CR-2208.

deep minimum epoch between SCs 23 and 24, the low latitudes of the streamer belt are characterized by lower electron temperature than in its mid-latitudes. A similar behavior is seen in CR-2208, belonging to the end of the declining phase of SC 24, but having a somewhat less axisymmetric structure this characteristic is not so obvious. This thermodynamic structure of the streamer have been reported for other solar minimum rotations in previous DMT works (Lloveras *et al.*, 2017; Nuevo *et al.*, 2013; Vásquez, Frazin, and Manchester, 2010).

For both target rotations, Figure 3 shows latitude-longitude maps of the DMT measure R defined by Equation 4, at the same three heights shown in Figures 2 and 3. In most of the coronal volume of the DMT grid the agreement between the tomographic and synthetic FBEs is $\lesssim 1\%$. The notable exception is to be found in the CHs of the target rotation analysed based on AIA data. A similar results was found in the two existing DMT works based on data provided by the AIA instrument (Nuevo *et al.*, 2015; Mac Cormack *et al.*, 2017). This point is further discussed below.

To characterize the DMT results in different magnetic structures, we traced $\sqrt{N_m^2}$ and T_m along the magnetic field lines of the AWSoM model. For both rotations, all legs that meet the criteria listed in Section 2.3 were selected. For each leg, the data points of electron density and electron mean temperature as a function of height were fitted to the Equations 5 and 6. As a result, the electron density $N_0(r = 1.0 R_\odot)$ and scale height λ_N were computed for each leg, as

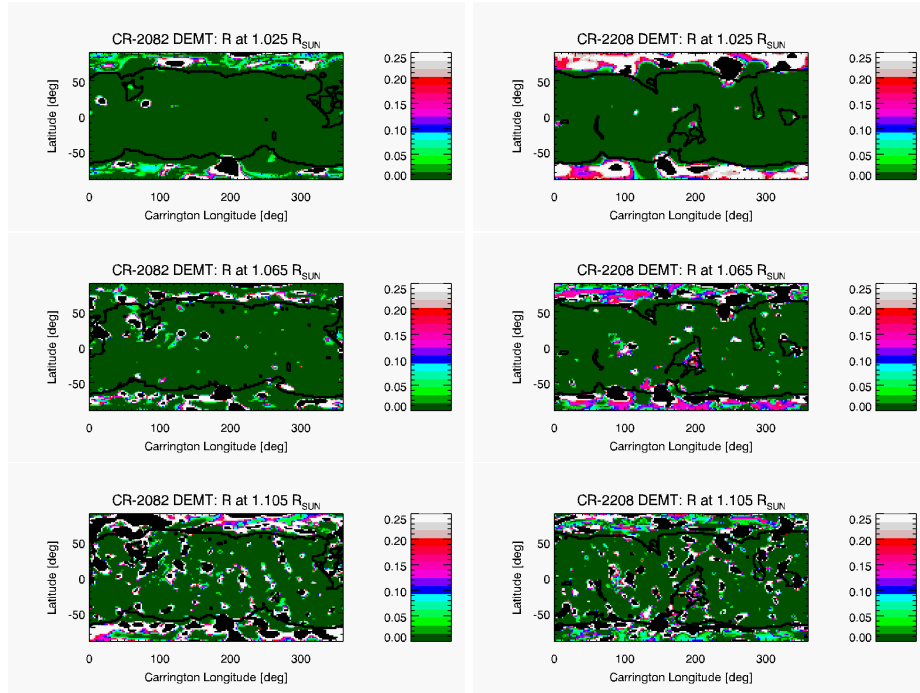


Figure 3. Carrington maps of the measure R defined by Equation 4, for CR-2082 (left panels) and CR-2208 (right panels), at heights 1.025, 1.065 and 1.105 R_{\odot} , from top to bottom.

well as the temperature gradient $\nabla_r T_m$, and the height-averaged (along the leg) electron temperature $\langle T_m \rangle$.

For both target rotations, the top panels of Figure 4 show the latitude-longitude location (at heliocentric height $r = 1.105 R_{\odot}$) of all traced field line legs for which criterion (i) of Section 2.3 is met. Open legs are indicated in gray color and closed ones in black color. For each leg, the fits to tomographic temperature and density were applied, as given by Equations 5-6. Considering the DMT data points and the resulting fits along each leg, the bottom panels of Figure 4 show the latitude-longitude location of the subset for which also both criteria (ii) and (iii) of Section 2.3 are met. Using a four-color code, type 0, I, II and III legs are shown in blue, red, magenta and cyan color, respectively. Of the ≈ 44000 legs selected for CR-2082, 20% are type 0, 31% are type I, 23% are type II and 26% type III. On the other hand, of the ≈ 44000 legs selected for CR-2208, 10% are type 0, 43% are type I, 30% are type II and 17% type III.

Type 0 (small down) legs mainly populate the equatorial latitudes. This kind of structure was originally found by Huang *et al.* (2012), and their existence was shown to be anti-correlated with the solar activity level around the solar minimum between SCs 23 and 24 by Nuevo *et al.* (2013). Later on, Lloveras *et al.* (2017) showed that equatorial down loops in streamers were also to be found in the deep minimum between SCs 23 and 24. Here, we verify the existence of this type of structure for the two target rotations. The relatively smaller

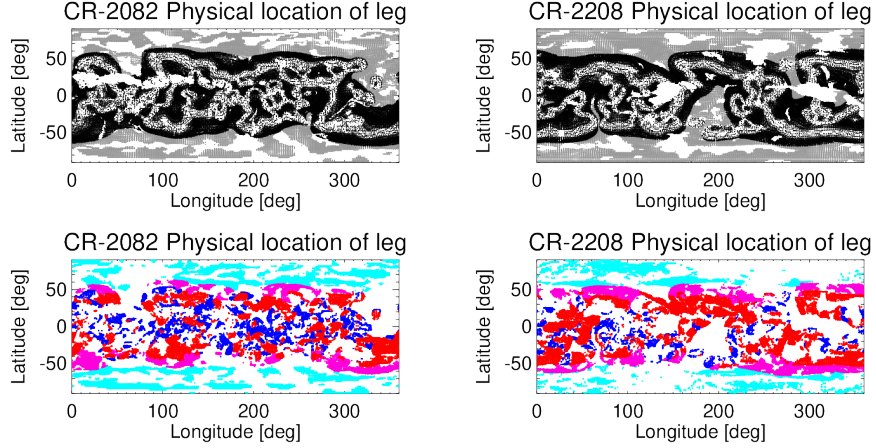


Figure 4. *Top panels:* latitude-longitude location at heliocentric height $r = 1.105 R_{\odot}$ of all open (grey color) and closed (black color) traced field line legs for which criterion (i) of Section 2.3 is met, for both CR-2082 (left) and CR-2208 (right). *Bottom panels:* latitude-longitude location of the subset for which also both criteria (ii) and (iii) of Section 2.3 are met. The location of type 0, I, II and III legs is shown in blue, red, magenta and cyan color, respectively.

population of down legs seen in CR-2208, as compared to CR-2082, is consistent with the aforementioned results by Nuevo *et al.* (2013). Type I (small up) mainly populate the mid-latitudes, while type II (large up) legs are mostly very large trans-equatorial field lines forming the envelope of the streamer belt. Finally, type III (open) legs populate the CHs.

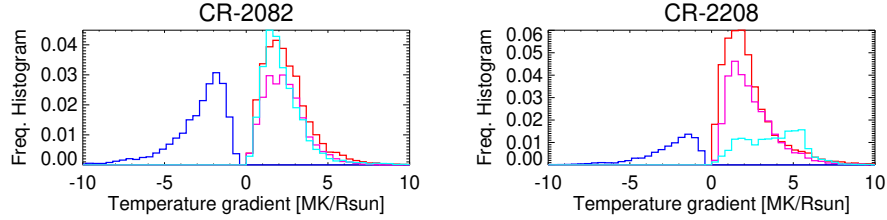


Figure 5. Frequency histograms of the temperature radial gradient for the four types of legs in Figure 4 (using the same color code) for CR-2082 (left panel) and CR-2208 (right panel).

Figure 5 shows frequency histograms of $\nabla_r T_m$ for legs of type 0, I, II and III. The lack of population around values close to zero is due to the requirement $|\rho(T, r)| > 0.5$ which discards quasi-isothermal legs. For both rotations, the median value of the temperature radial gradient is $\text{Md}(\nabla_r T_m) \approx -2.5, +2.3$ and $+2.4 \text{ MK/R}_{\odot}$ for legs of type 0, I and II, respectively.

The notable difference between both rotations is the characteristic value $\text{Md}(\nabla_r T_m) \approx +4.5 \text{ MK/R}_{\odot}$ for legs of type III for CR-2208. This is related to the much larger R score for the DMT results along CH legs for CR-2208. In this case, DMT performs poorly in modeling a LDEM that predicts the

tomographic FBEs with reasonable accuracy. Indeed, visual inspection of the DENT temperature maps for CR-2208 in Figure 3, reveals that in most of the CH region the result for T_m below height $1.105 R_\odot$ is quite uniform and artificially low. As it turns out, around and above height this height the score R is lower and the temperature results are more reliable. As a result, the temperature gradient along these legs is artificially larger, with the linear fit trying to simultaneously fit the artificially low values of T_m at lower heights. In general, the DENT results in the CH region based on AIA data are thus much less reliable than in the rest of the analysis. We will return to this point in the conclusion section.

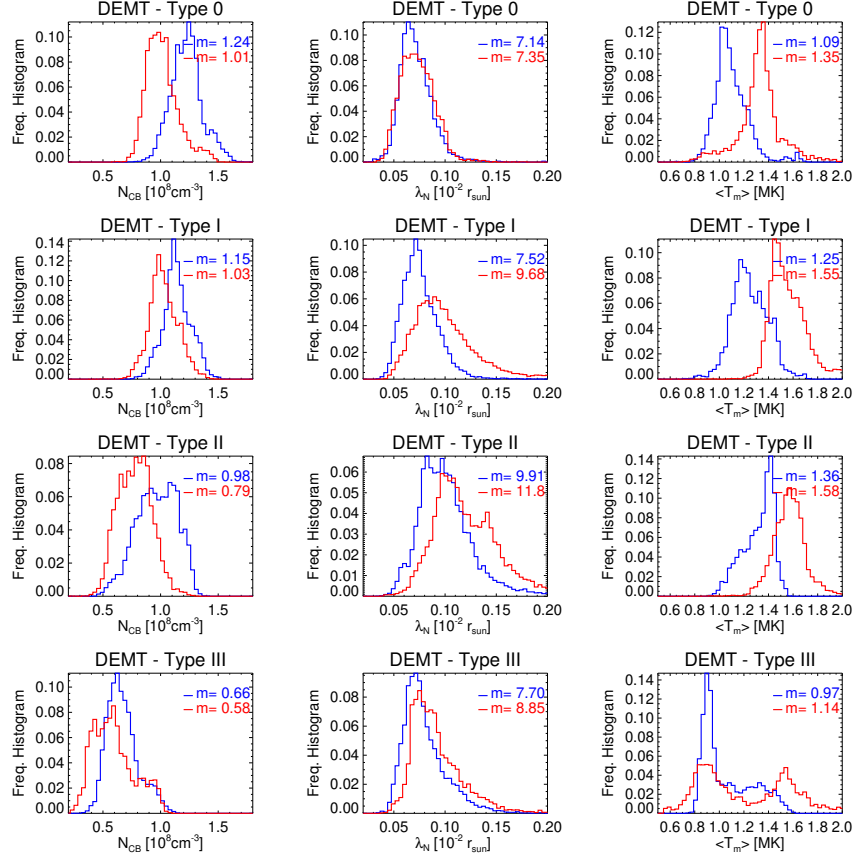


Figure 6. Statistical distribution of DENT results for rotations CR-2082 (blue) and CR-2208 (red) traced along legs of type 0, I, II and III (from top to bottom), as defined in Section 2.3. From left to right: electron density $N_{CB} \equiv \sqrt{N_m^2}(r = 1.055 R_\odot)$, electron density scale height λ_N , and loop-averaged temperature $\langle T_m \rangle$. In each panel the median value m is indicated.

For both rotations, Figure 6 shows, in a statistical fashion, the DENT results traced along field lines discriminated by leg type. From top to bottom results are shown for type 0 to type III legs, respectively. From left to right the panels show the statistical distribution of $N_{CB} \equiv \sqrt{N_m^2}(r = 1.055)$ (the lowest height

where the AWSOM results are consistent with coronal conditions), λ_N and $\langle T_m \rangle$, with the median value m indicated in each plot.

Table 1 summarizes a quantitative comparative analysis between the results of the two target rotations. For CR-2082 quantities are expressed as absolute values, while for CR-2208 they are informed as a percentual variation relative to the corresponding results for CR-2082. The following major results, both concerning the structure of each rotation individually as well as their comparison, can be drawn.

Table 1. Median value (indicated as “Md”) of the statistical distribution of N_{CB} , λ_N , and $\langle T_m \rangle$ for each coronal type of legs defined in Section 2.3. For CR-2082 values are expressed in absolute terms, while for CR-2208 they are informed as a percentual variation relative to the CR-2082 value.

Type	Md(N_{CB}) [10^8 cm^{-3}]	Md(λ_N) [10^{-2} R_\odot]	Md($\langle T_m \rangle$) [MK]
0	1.24 (-19%)	7.1 (+ 3%)	1.09 (+24%)
I	1.15 (-10%)	7.5 (+29%)	1.25 (+24%)
II	0.98 (-20%)	9.9 (+19%)	1.36 (+16%)
III	0.66 (-12%)	7.7 (+15%)	0.97 (+18%)

Throughout the magnetically closed region of both rotations, type 0, I and II legs, associated to increasingly outer layers of the equatorial streamer belt, exhibit progressively decreasing coronal base density, increasing density scale height, and increasing electron temperature. In both rotations also, type III legs in the CHs are characterized by sub-MK temperatures, and electron density values of order $\approx 1/2$ of those observed for the type 0 and type I legs in the core of the equatorial streamer.

A comparison of the results between the two rotations shows that, compared to CR-2082, target rotation CR-2208 was characterized by $\approx 10 - 20\%$ lower values of the electron density at the coronal base, $\approx 5 - 30\%$ larger values of density scale height, and $\approx 5 - 25\%$ larger values of the electron temperature.

To analyze the loop-integrated energy flux quantities introduced in Section 2.3, we selected closed loops for which both legs have the same sign of the radial gradient of the electron temperature $\nabla_r T_m$. In this way, according to the classification of both its legs, each given loop was classified as of type 0 (small down loop), I (small up loop), or II (large up loop). For both target rotations, and for loops of type 0, I and II, Figure 7 shows the frequency histogram of the loop-integrated energy flux quantities ϕ_r , ϕ_c and ϕ_h in blue, green and red color, respectively.

For both rotations, the value of the loop-integrated radiative power E_r , measured by the quantity ϕ_r , is largest for loops of type 0. This is due to $E_r \propto N_e^2 \Lambda(T_e)$, with both factors contributing to maximize E_r for loops of type 0. As shown in Figure 6 and Table 1, loops of type 0 are characterized by the largest values of electron density. Also, in the range of sensitivity of the EUVI and AIA

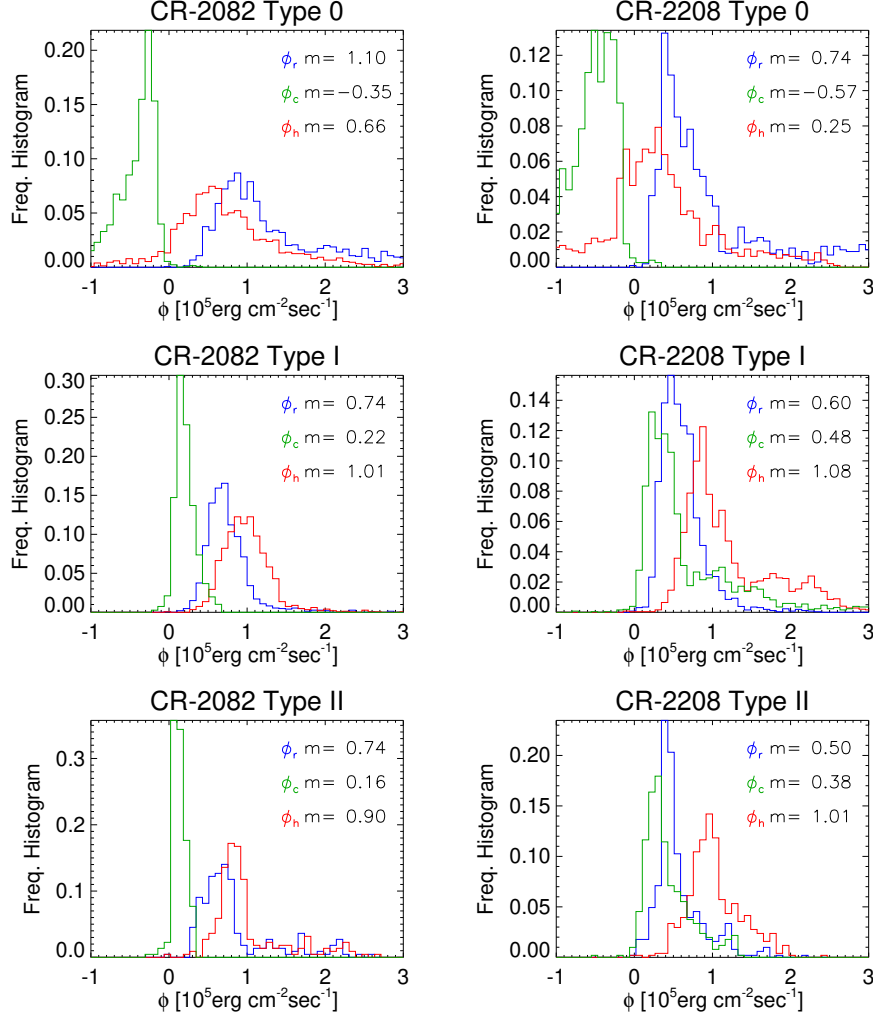


Figure 7. Statistical results of the loop-integrated energy flux quantities ϕ_r , ϕ_c , and ϕ_h in colors blue, red and green, respectively for CR-2082 (left) and CR-2208 (right). From top to bottom, panels show the results for loops of type 0, I and II, which are loops for which both legs meet the criteria from Section 2.3.

instruments, namely 0.5–3.0 MK (Nuevo *et al.*, 2015), the radiative loss function $\Lambda(T)$ has a local maximum at $T_c \approx 1$ MK. According to Figure 6, loops of type 0, I and II are characterized by values of temperature that are progressively larger and farther from the value T_c , for both rotations.

The sign of the quantity ϕ_c depends on that of the conductive flux F_c . Equations 8 and 12 imply that down loops (type 0) and up loops (type I and II) are characterized by $\phi_c < 0$ and $\phi_c > 0$, respectively, as verified in Figure 7.

Adding the radiative and conductive terms, the characteristic energy input flux at the coronal base is in the range $\phi_h \approx 0.5 - 1.5 \times 10^5 \text{ erg cm}^{-2} \text{ s}^{-1}$, depending on the rotation and the type of loop, matching the values reported by Mac Cormack *et al.* (2017). Note that for type 0 loops there is a marginal population characterized by the unphysical result $\phi_h < 0$. As shown by Mac Cormack *et al.* (2017), this affects only the smallest sized loops of the type 0, and it is most probably due to the limited temperature sensitivity of the instrumental passbands. The radiative loss term is here calculated based on plasma emission detected by three coronal bands of EUVI or AIA. Though accounting for most of the coronal plasma, there surely is additional emission out of the instrumental sensitivity range. As a result, the positive term ϕ_r is most likely underestimated, leading to values $\phi_h < 0$ in loops of type 0, being characterized by $\phi_c < 0$.

3.2. Comparison of the DMT and AWSoM Models

Figure 8 shows carrington maps of the radial magnetic field (B_r) for both rotations at $1.005 R_\odot$. Both maps clearly show the large-scale dipolar field, characteristic of solar minimum conditions. Differences between both maps are observed in the sub-polar latitudes, due to the different treatments applied there by the GONG (CR-2082) and the ADAPT-GONG (CR-2208) maps.

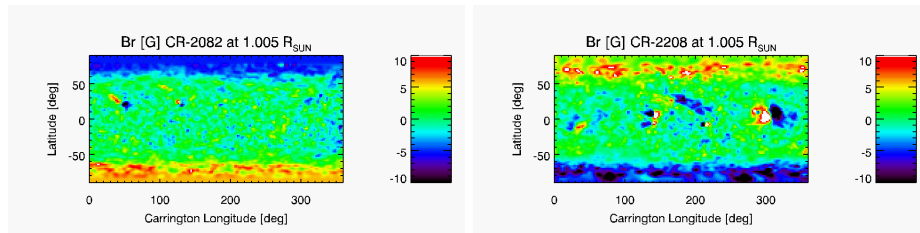


Figure 8. Carrington maps of the radial magnetic field B_r of the AWSoM model at $1.005 R_\odot$ for CR-2082 (left) and CR-2208 (right).

For both target rotations, Figures 9 and 10 show latitude-longitude maps of the AWSoM electron density and temperature. Maps are shown at the same three heights selected for visualization of the DMT results in Figures 1 and 2. Thick-black curves indicate the magnetic open/closed boundaries based on the magnetic field of the AWSoM model. Visual inspection of these maps shows that the AWSoM model for both rotations is highly axisymmetric, as the tomographic model.

As described in Section 2.2, the AWSoM model includes an artificially thick TR, achieving coronal conditions above height $\approx 1.06 R_\odot$. Indeed, the top panels in Figures 9 and 10, at height $1.025 R_\odot$, clearly do not represent coronal conditions (although we include them here for completeness). When compared to DMT results (Figures 1 and 2), the latitude-longitude maps of the AWSoM model for heights 1.065 and $1.105 R_\odot$ capture well the denser and hotter equatorial streamer belt surrounded by the less dense and colder CHs. Furthermore, for both target rotations, the temperature maps show the low latitudes of the

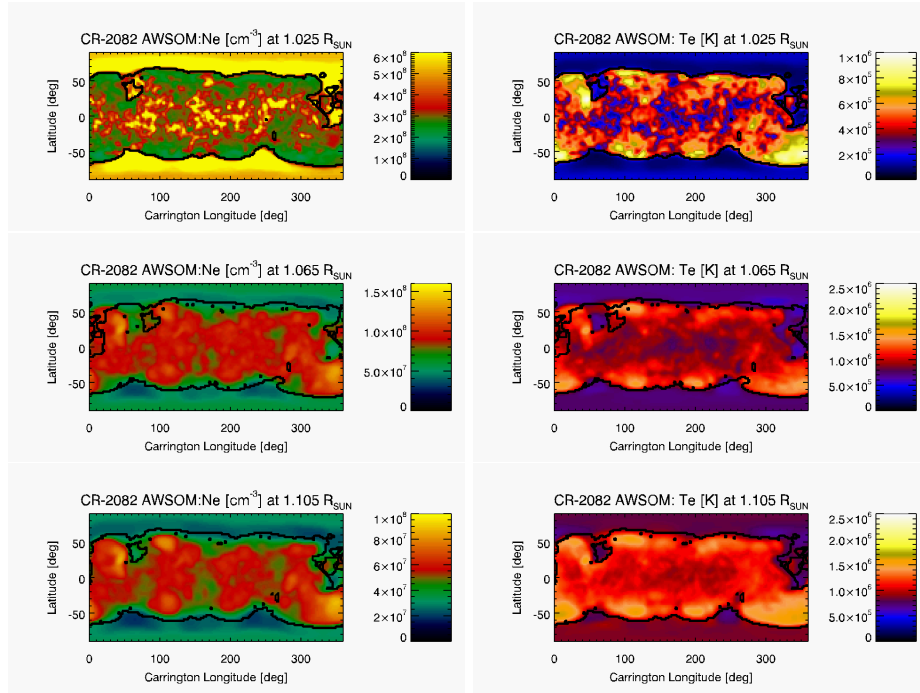


Figure 9. Carrington maps of density (left panels) and temperature (right panels) obtained with AWSoM model for the same three heights shown in Figure 1.

equatorial streamer belt to be characterized by lower temperatures than its mid-latitudes, as also seen in the DMT results. The latitude-longitude maps of the AWSoM and DMT results are shown in the same units and scales, so that a visual comparison among them already reveals similar values of electron density and temperature in both models.

Being highly axisymmetric target rotations, the longitude-averaged latitudinal profile of the results of both models is an informative way to compare their large-scale structure. Such comparison is shown in Figure 11 at height 1.105 R_⊙, with top panels comparing electron density and mid panels electron temperature. The longitude-averaged latitudinal profile of B_r is shown in the bottom panels. In these longitude-averaged profiles, longitudes containing ARs or low latitude CHs were excluded. In each panel the averaged latitudinal variation for the DMT model is shown in solid-line style, while the result for the AWSoM model is shown in dashed-line style. Left panels show the comparison for CR-2082 (in blue) and right panels for CR-2208 (in red). In each panel the vertical black lines denote the corresponding longitude-averaged latitude of the open-close boundary in both hemispheres.

Several details from Figure 11 are worth being highlighted. Firstly, at most latitudes the overall agreement of the electron density of both models is within $\approx 20\%$ for CR-2082, and $\approx 5\%$ for CR-2208. The noticeable exception is to be found near the open/closed boundaries of both target rotations, where the

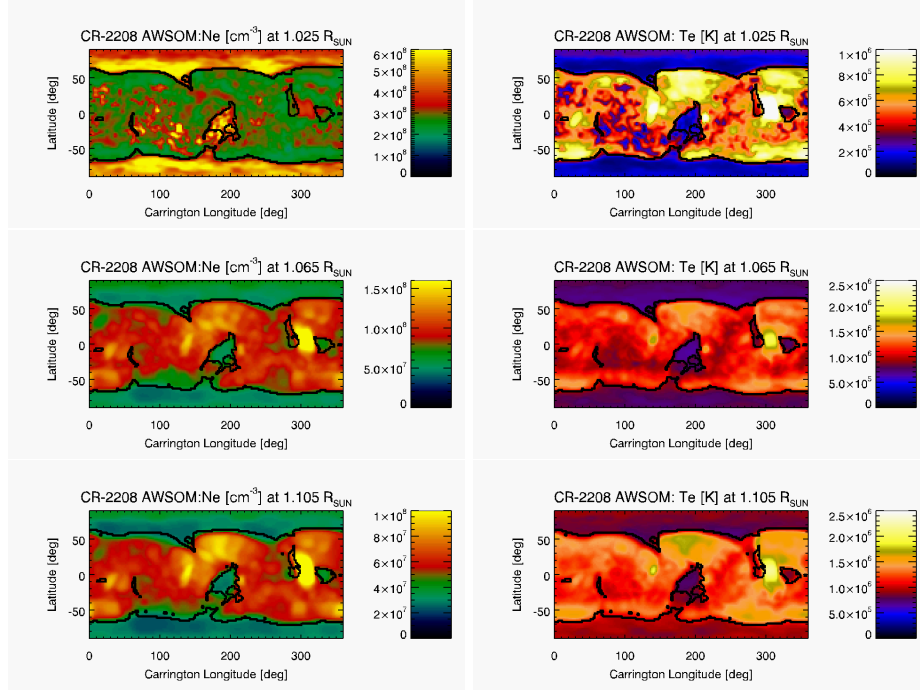


Figure 10. Same as Figure 10 for CR-2208.

disagreement between both models can be up to twice as much. In the case of the electron temperature, for both target rotations the models agree within $\approx 15\%$ at all latitudes of the streamer belt, showing larger discrepancies in the CHs. Secondly, for both target rotations, and for both models, these plots clearly show the relatively lower temperatures characterising the low-latitudes of the equatorial streamer belt compared to its mid-latitudes. Thirdly, for both target rotations, the latitude of the open/closed magnetic boundary in both hemispheres matches the location of the strongest latitudinal gradient of the DGMT electron density. Note this is not the case for the AWSOM model, that shows a minimum density at the open/closed boundary. Last, note that the DGMT electron density decreases from the open/closed boundary towards the poles (in both hemispheres of the two target rotations), while the AWSOM model shows the opposite trend. For comparison, note the behavior of B_r in the CHs, increasing from the open/closed boundary towards the poles for CR-2082, while showing local maxima around latitudes -75° and $+70^\circ$ in the case of CR-2208.

To characterize the results of the AWSOM model in distinct magnetic structures, its results for electron density and temperature were traced along its magnetic field lines. For each field line leg, the results were then fit to Equations 5 and 6, considering only data points above heliocentric height $1.055 R_\odot$. We then classified the traced legs into types I, II and III, according to the criteria described in Section 2.3. Legs of type 0 are not included for AWSOM, as in its

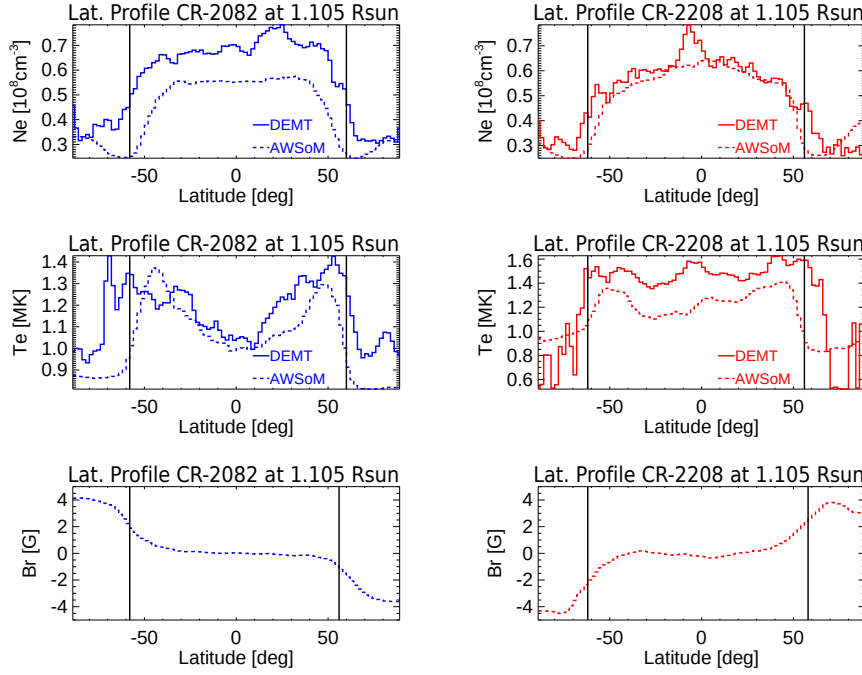


Figure 11. Longitude-averaged latitudinal dependence of the electron density (top panels), electron temperature (middle panels) and radial magnetic field B_r (bottom panels), for target rotations CR-2082 (blue color, left panels) and CR-2208 (red color, right panels) at $1.105 R_\odot$. Dashed lines correspond to AWSoM results while solid line to DENT. The vertical black line indicates the longitude-averaged latitudes of the open/closed magnetic boundary in both hemispheres.

current implementation it can not simulate down loops, a point we will discuss in the next section.

For both target rotations, the top panels of Figure 12 show the latitude-longitude location (at heliocentric height $1.105 R_\odot$) of all traced field line legs for which criterion (i) of Section 2.3 is met. That criterion is adapted here, requiring that at least five voxels of the tomographic grid are threaded by the leg. Open legs are indicated in gray color and closed ones in black color. For each leg, the fits to tomographic temperature and density were applied, as given by Equations 5 and 6. Considering the AWSoM data points and the resulting fits along each leg, the bottom panels of Figure 12 show the latitude-longitude location of the subset for which also both criteria (ii) and (iii) of Section 2.3 are met. Using a three-color code, type I, II and III legs are shown in red, magenta and cyan color, respectively. This figure is to be compared with the corresponding Figure 4 for DENT results. It is readily seen that the AWSoM maps are more populated than those of DENT. This is due to the 3D MHD model having electron density and temperature fields spatially smoother than those of DENT.

For target rotation CR-2082, Figure 13 shows the statistical distribution of the results of the DENT (solid line-style) and AWSoM (dashed line-style) models

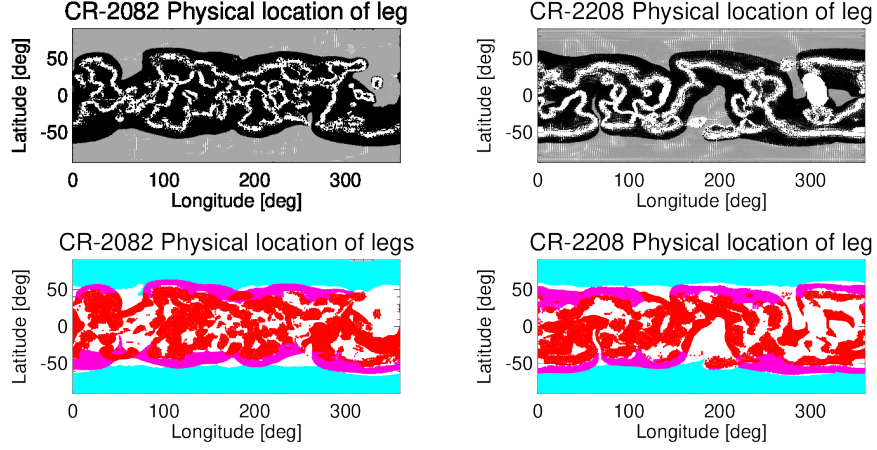


Figure 12. Same as Figure 4, but using the density and temperature of the AWSoM model to classify its legs in types I, II and III. The model does not exhibit legs of type 0.

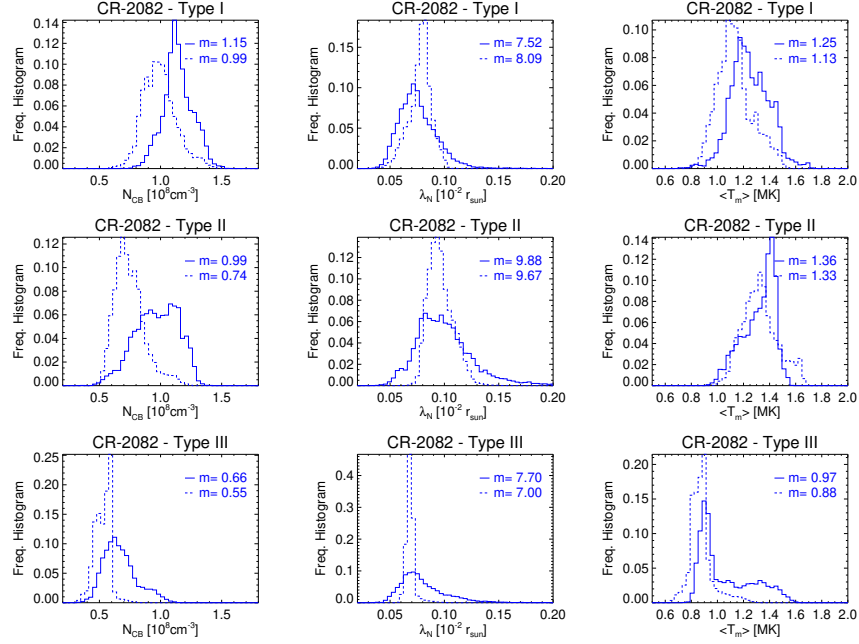


Figure 13. Statistical distribution of the results of the DENT (solid line-style) and AWSoM (dashed-line style) models traced along legs of type I, II and III (from top to bottom), as defined in Section 2.3. From left to right: electron density at the lowest coronal height of the AWSoM model $N_e(r = 1.055 R_\odot)$, electron density scale height λ_N , and leg-averaged electron temperature $\langle T_m \rangle$. In each panel the median values m are indicated.

traced along legs of type I, II and III (from top to bottom), as defined in Section 2.3. From left to right: electron density at the lowest coronal height of the AWSoM model $N_{CB} \equiv N_e(r = 1.055 R_\odot)$, electron density scale height λ_N , and leg-averaged electron temperature $\langle T_m \rangle$. In each panel the median values m are indicated. Figure 14 shows the same analysis for target rotation CR-2208.

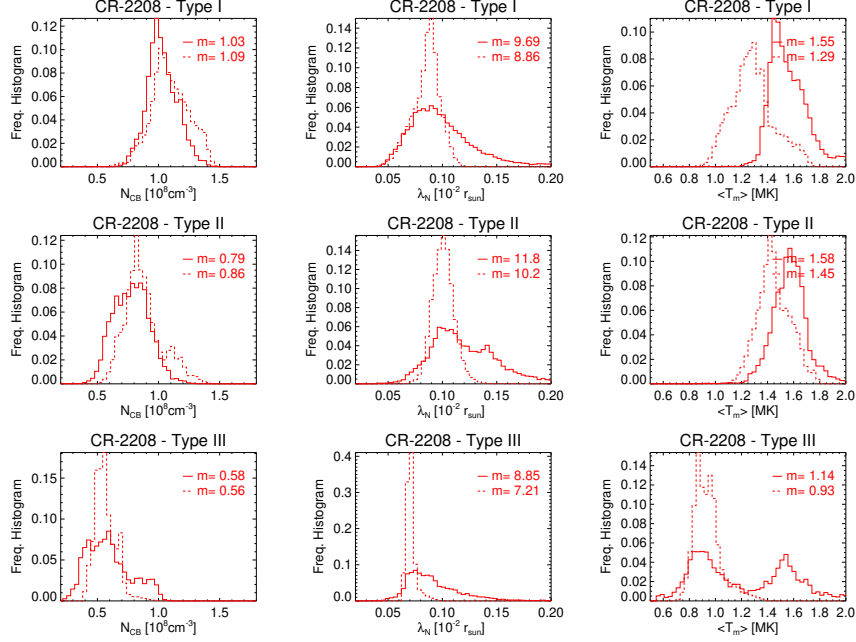


Figure 14. Same as Figure 13 for CR-2208.

For the two target rotations, Table 2 summarizes a quantitative comparative analysis between the results of the DMT and AWSoM models based on the results shown in Figures 13 and 14. The DMT results are expressed as absolute values, while the ASWSOM results are informed as a percentual variation relative to the corresponding result for DMT. The following major results can be drawn.

For target rotation CR-2082, the median value of the electron density N_{CB} of both models agree within $\approx 10 - 25\%$, depending of the type of leg, with the largest discrepancy found for legs of type II (near the open/closed boundary). The median value of the scale height λ_N agree within $\approx 10\%$ in all regions. The leg-averaged electron temperature $\langle T_m \rangle$ of both models also agree within 10% in all regions. For target rotation CR-2208 the agreement of the median value of N_{CB} and λ_N of both models is within 10% , while median values of $\langle T_m \rangle$ agree within 15% . These detailed results, being consistent with the large-scale comparison provided in Figure 11, show in detail how the AWSoM model performs compared to DMT in different magnetic structures.

Finally, to provide a graphical comparison of both models across the full range of heliocentric heights covered by the DMT results, Figure 15 shows the average fits of $N_e(r)$ and $T_e(r)$ for legs of type I (red), II (magenta), and III (cyan) for

Table 2. Median value (indicated as “Md”) of the statistical distribution of N_{CB} , λ_N , and $\langle T_m \rangle$ for each coronal type of leg defined in Section 2.3. DMT values are expressed in absolute terms, while AWSoM results are informed as a percentual variation relative to the corresponding DMT value.

Type	Md(N_{CB}) [10^8 cm^{-3}]	Md(λ_N) [$10^{-2} R_\odot$]	Md($\langle T_m \rangle$) [MK]
CR-2082			
I	1.15 (-14%)	7.5 (+ 8%)	1.25 (-10%)
II	0.99 (-25%)	9.9 (- 2%)	1.36 (- 2%)
III	0.66 (-17%)	7.0 (- 9%)	0.97 (- 9%)
CR-2208			
I	1.03 (+ 6%)	9.7 (- 8%)	1.55 (-17%)
II	0.79 (+ 9%)	11.8 (-14%)	1.58 (- 8%)
III	0.58 (- 3%)	8.9 (-18%)	1.14 (-18%)

both target rotations. In each panel the DMT and AWSoM results are plotted in solid and dashed line styles, respectively.

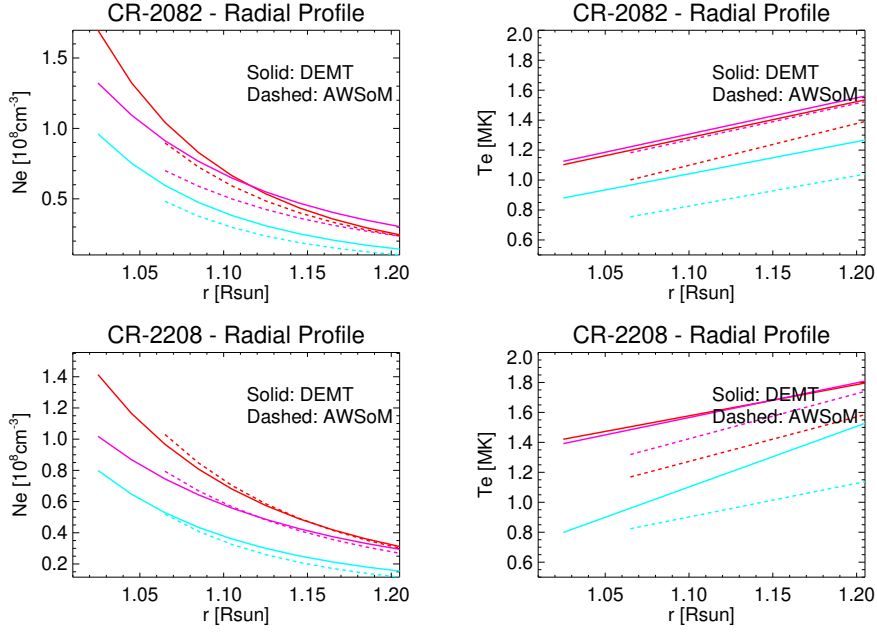


Figure 15. Average fits to $N_e(r)$ (left panels) and $T_e(r)$ (right panels) for legs of type I (red), II (magenta), and III (cyan), for CR-2082 (top panels) and CR-2208 (bottom panels). Solid lines correspond to DMT results while dashed lines correspond to AWSoM results.

As discussed above, Figure 11 shows that the longitude-averaged latitudinal profile of the DENT electron density in the CHs decreases towards the poles. Figure 16 below shows the longitude-averaged AWSoM radial wind speed V_r at $6 R_\odot$, where all field lines are open. The heliocentric current sheet (HCS) location is indicated by the minimum of the speed curve. For each rotation, all velocity data points to the south of the HCS position map down to the southern CH in Figures 11. Similarly, all velocity data points to the north of the HCS position map down to the northern CH in Figures 11. This clearly shows an anti-correlation between the DENT electron density at low heights and the AWSoM wind speed at larger heights.

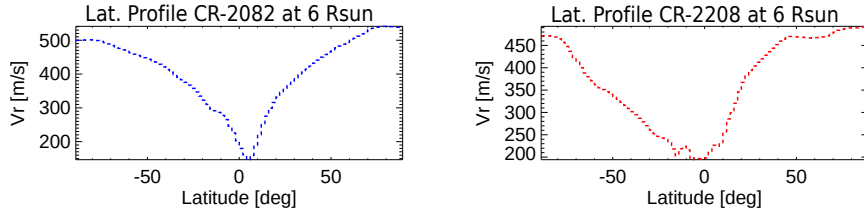


Figure 16. Longitude-averaged latitudinal dependence of the AWSoM model wind speed V_r at $6.0 R_\odot$ for CR-2082 (left panel) and CR-2208 (right panel).

4. Discussion and Conclusions

We carried out the 3D DENT reconstruction and MHD modeling of the inner solar corona for two target rotations, CR-2082 and CR-2208. The first target belongs to the deep minimum epoch between SCs 23 and 24, while the latter belongs to the end of the declining phase of SC 24. The present work introduces two improvements in the implementation of DENT, namely the use of only off-limb data in the EUV images, and the inclusion of a 3D regularization scheme. As a result of the former, artifacts introduced by coronal dynamics are mitigated, and as a result of the latter, tomographic reconstructions behave more smoothly close to the radial boundaries of the computational grid when compared to previous reconstructions. The MHD model used is here the latest version of the AWSoM component of the SWMF suite.

Based on the magnetic field of AWSoM model and the results of the DENT model for electron density and temperature, we classified coronal structures in four different types. **Small loop legs** in the core of the streamer belt are classified in down/up types according to their temperature decreasing/increasing with height (dubbed type 0/I). **Large closed legs** of type up that form the envelope of the streamer belt (dubbed type II), and open field lines of type up populating the CHs (dubbed type III).

Concerning the DENT reconstructions, Figure 4 shows that, for both target rotations, magnetic field lines of type 0, I and II are associated to increasingly outer layers of the equatorial streamer belt. Figure 6 and Table 1 report in

3D quantitative detail how these progressively outer magnetic structures exhibit progressively decreasing coronal base density, increasing density scale height, and increasing electron temperature. For both target rotations we find that down legs populate the low latitudes of the streamer belt, while up legs dominate its mid-latitudes. Also, in the case of CR-2082 the fraction of down legs is significantly larger than for CR-2208. These findings are consistent with previous studies by Huang *et al.* (2012) and Nuevo *et al.* (2013). In the case of the latter, they include in their analysis target CR-2081, which is a rotation almost identical to our target CR-2082. Our results for target CR-2082 compare very well with those of Nuevo *et al.* (2015) and Lloveras *et al.* (2017) for target CR-2081. As our study uses the improved version of the DENT technique, such comparison provided a consistency check for the changes implemented in the DENT technique.

For both target rotations, type III field lines in the CHs are characterized by sub-MK temperatures, and electron density values of order $\approx 1/2$ of those observed for the type 0 and type I lines in the core of the equatorial streamer. In the case of the DENT reconstruction based on AIA data we show that, in a substantial fraction of the voxels of the CHs, the technique performs poorly in modeling an LDEM that predicts the tomographic emissivity in each EUV band with reasonable accuracy. As a result, DENT results based on AIA data are less reliable CHs. This was already found by the existing two previous DENT works based on AIA data (Nuevo *et al.*, 2015; Mac Cormack *et al.*, 2017). The source of this distinct performance of DENT when applied to EUVI or AIA data is related to the TRFs of the respective filter sets. We are currently implementing an improved LDEM determination algorithm to deal with this issue that will be used in a follow up article.

In comparing the DENT results obtained for the two selected targets, we highlight they rely on data provided by two different instruments, namely EUVI and AIA for CR-2082 and CR-2208, respectively. In order to quantify the systematic difference of the DENT products due to the different filter sets of both instruments, Nuevo *et al.* (2015), who were the first to apply DENT to AIA data, analysed a single target using both instruments independently. They found that while the density products are essentially equal, the temperature product of DENT based on AIA data is systematically 8% larger than the one based on EUVI data, *i.e.* $T_m^{(AIA)} / T_m^{(EUVI)} \approx 1.08$. Considering such correction, Figure 6 and Table 1 indicate that CR-2208 was characterized by temperatures $\approx 10 - 15\%$ larger relative to CR-2082 throughout the streamer belt region. As for the electron density products, CR-2208 was found to be $\approx 15 - 20\%$ less dense than CR-2082 throughout the streamer belt region. These systematic differences are around or beyond the uncertainty level in the DENT products due to systematic sources (radiometric calibration and tomographic regularization), that Lloveras *et al.* (2017) estimated to be $\Delta T_m \approx 10\%$ and $\Delta \sqrt{N_m^2} \approx 5\%$.

In the streamer belt region we combined the DENT results and the AWSOM magnetic model to infer the energy input flux ϕ_h at the coronal base required to maintain stable coronal loops. To this end, we applied the technique developed by Mac Cormack *et al.* (2017). We found characteristic values in the range $\phi_h \approx 0.5 - 1.5 \times 10^5 \text{ erg cm}^{-2} \text{ s}^{-1}$, depending on the rotation and the type of loop, matching the values reported by Mac Cormack *et al.* (2017). Based on

spectroscopic data of the EIS instrument in quiet-Sun regions Hahn and Savin (2014) showed that, if the observed non-thermal broadening are assigned to Alfvén waves, their energy flux at the coronal base is estimated to be in the range $\approx 1.5 - 2.5 \times 10^5 \text{ erg cm}^{-2} \text{ s}^{-1}$. A large fraction of the coronal base energy input flux ϕ_h estimated in this work, or even its totality, could then be accounted for by Alfvén waves.

Results of the AWSoM model were compared to those of the DENT reconstructions in the range of coronal heights simultaneously covered by both models, namely $\approx 1.05 - 1.20 R_\odot$. In its current implementation, the AWSoM model can not reproduce down loops (type 0), so the comparison is restricted to type I, II and III field lines. The detailed comparison shown in this work can be summarized as follows. For CR-2082, the electron density of both models agree within $\approx 20\%$ in most regions, while for CR-2208 the agreement is within $\approx 5\%$. The noticeable exception is to be found near the open/closed boundaries of both target rotations, where the disagreement between both models can be up to twice as much. In the case of the electron temperature, both models agree within $\approx 10 - 15\%$ in all regions, for both target rotations, with larger discrepancies in the CHs. This level of agreement between both models (within or slightly beyond the uncertainty level of DENT results) is considerably better than that reported in previous works. Jin *et al.* (2012) and Oran *et al.* (2015), who used previous versions of the AWSoM model, reported electron density values of the AWSoM model differing by $\approx 50\%$ compared to the DENT reconstructions, both in the equatorial streamer and CH regions.

The overall better match of the results of the current version of the AWSoM model when compared to DENT reconstructions is partly due to the improved energy partitioning scheme of the model, described in Section 2.2. Note also that the simulation of CR-2082 used GONG maps as boundary condition, while the simulation of CR-2208 used the improved ADAPT-GONG maps. This is most probably the cause that the results of the AWSoM model show a more accurate match to the DENT reconstructions in the case of CR-2208.

Within the excellent quantitative match between both models summarized in the previous paragraph, there are some qualitative agreements and disagreements worth noticing. For both target rotations, the AWSoM model reproduces the relatively lower temperatures found by DENT to characterize the low-latitudes of the equatorial streamer belt compared to its mid-latitudes. On the other hand, while the latitude of the open/closed magnetic boundary in both hemispheres matches the location of the strongest latitudinal gradient of the DENT electron density (physically expected in transitioning from magnetically closed to open regions), this is not the case for the AWSoM model, that shows a minimum density at the open/closed boundary. Also, while the DENT electron density decreases from the open/closed boundary towards the poles (in both hemispheres of the two target rotations), as expected in transitioning from the source region of the slow to the fast component of the solar wind, the AWSoM model shows the opposite trend. This behavior is notoriously opposite to that reported in the AWSoM model version used by Oran *et al.* (2015), in which the electron density decreases from the open/closed boundary towards the poles. These unphysical characteristics of the results of the AWSoM model in the range

of low heights analysed here ($r \lesssim 1.2R_{\odot}$), may be traced down to the less reliable values of B_r provided by both the GONG and ADAPT-GONG maps at subpolar latitudes, rather than a limitation of the model itself. This will be further investigated in a follow up article focusing on the current deep minimum epoch, during which the large-scale corona shows the simplest possible structure.

A detailed empirical description of the 3D thermodynamic structure of the inner corona at a global scale is currently only possible with tomographic techniques, such as DENT. Using tomographic results for continuous validation of 3D MHD models is of high relevance for the continued improvement of models. In follow up articles we will carry out the 3D DENT reconstruction and MHD modeling of new target rotations selected from the current solar minimum epoch between SCs 24 and 25, as well as rotation CR-2219 corresponding to the July 2nd 2019 total solar eclipse.

Acknowledgments D.G.Ll. and C.M.C. acknowledge CONICET doctoral fellowships (Res. Nr. 4870) to IAFE that supported their participation in this research. D.G.Ll, A.M.V., F.A.N. and C.M.C. acknowledge ANPCyT grant 2016/0221 to IAFE that partially supported their participation in this research. A.M.V. also acknowledges UBACyT grant 20020160100072BA to DCAO-UBA to FCEyN-UBA and IAFE that partially supported his participation in this research.

Disclosure of Potential Conflicts of Interest: The authors declare that they have no conflicts of interest.

References

- Arge, C.N., Henney, C.J., Koller, J., Compeau, C.R., Young, S., MacKenzie, D., Fay, A., Harvey, J.W.: 2010, Air Force Data Assimilative Photospheric Flux Transport (ADAPT) Model. In: Maksimovic, M., Issautier, K., Meyer-Vernet, N., Moncuquet, M., Pantellini, F. (eds.) *Twelfth International Solar Wind Conference, American Institute of Physics Conference Series* **1216**, 343. DOI. ADS.
- Aschwanden, M.J.: 2004, *Physics of the Solar Corona. An Introduction*. ADS.
- Aschwanden, M.J., Schrijver, C.J.: 2002, Analytical Approximations to Hydrostatic Solutions and Scaling Laws of Coronal Loops. *Astrophys. J. Suppl.* **142**(2), 269. DOI. ADS.
- Chandran, B.D.G., Dennis, T.J., Quataert, E., Bale, S.D.: 2011, Incorporating Kinetic Physics into a Two-fluid Solar-wind Model with Temperature Anisotropy and Low-frequency Alfvén-wave Turbulence. *Astrophys. J.* **743**(2), 197. DOI. ADS.
- Del Zanna, G., Dere, K.P., Young, P.R., Landi, E., Mason, H.E.: 2015, CHIANTI - An atomic database for emission lines. Version 8. *Astron. Astrophys.* **582**, A56. DOI. ADS.
- Frazin, R.A.: 2000, Tomography of the Solar Corona. I. A Robust, Regularized, Positive Estimation Method. *Astrophys. J.* **530**, 1026. DOI. ADS.
- Frazin, R.A., Vásquez, A.M., Kamalabadi, F.: 2009, Quantitative, Three-dimensional Analysis of the Global Corona with Multi-spacecraft Differential Emission Measure Tomography. *Astrophys. J.* **701**, 547. DOI. ADS.
- Hahn, M., Savin, D.W.: 2014, Evidence for Wave Heating of the Quiet-Sun Corona. *Astrophys. J.* **795**(2), 111. DOI. ADS.
- Henney, C.J., Toussaint, W.A., White, S.M., Arge, C.N.: 2012, Forecasting F_{10.7} with solar magnetic flux transport modeling. *Space Weather* **10**, S02011. DOI. ADS.
- Huang, Z., Frazin, R.A., Landi, E., Manchester, W.B., Vásquez, A.M., Gombosi, T.I.: 2012, Newly Discovered Global Temperature Structures in the Quiet Sun at Solar Minimum. *Astrophys. J.* **755**, 86. DOI. ADS.

- Jin, M., Manchester, W.B., van der Holst, B., Oran, R., Sokolov, I., Toth, G., Gombosi, T.I., Vourlidas, A., Liu, Y., Sun, X.: 2012, Simulate the Coronal Mass Ejection on 2011 March 7 from Chromosphere to 1 AU. In: *AGU Fall Meeting Abstracts* **2012**, SH33E. ADS.
- Landi, E., Young, P.R., Dere, K.P., Del Zanna, G., Mason, H.E.: 2013, CHIANTI - An Atomic Database for Emission Lines. XIII. Soft X-Ray Improvements and Other Changes. *Astrophys. J.* **763**, 86. DOI. ADS.
- Lemen, J.R., Title, A.M., Akin, D.J., Boerner, P.F., Chou, C., Drake, J.F., Duncan, D.W., Edwards, C.G., Friedlaender, F.M., Heyman, G.F., Hurlburt, N.E., Katz, N.L., Kushner, G.D., Levay, M., Lindgren, R.W., Mathur, D.P., McFeaters, E.L., Mitchell, S., Rehse, R.A., Schrijver, C.J., Springer, L.A., Stern, R.A., Tarbell, T.D., Wuelser, J.-P., Wolfson, C.J., Yanari, C., Bookbinder, J.A., Cheimets, P.N., Caldwell, D., Deluca, E.E., Gates, R., Golub, L., Park, S., Podgorski, W.A., Bush, R.I., Scherrer, P.H., Gumm, M.A., Smith, P., Aufer, G., Jerram, P., Pool, P., Soufli, R., Windt, D.L., Beardsley, S., Clapp, M., Lang, J., Waltham, N.: 2012, The Atmospheric Imaging Assembly (AIA) on the Solar Dynamics Observatory (SDO). *Solar Phys.* **275**, 17. DOI. ADS.
- Lionello, R., Linker, J.A., Mikić, Z.: 2009, Multispectral Emission of the Sun During the First Whole Sun Month: Magnetohydrodynamic Simulations. *Astrophys. J.* **690**(1), 902. DOI. ADS.
- Lithwick, Y., Goldreich, P., Sridhar, S.: 2007, Imbalanced Strong MHD Turbulence. *Astrophys. J.* **655**(1), 269. DOI. ADS.
- Lloveras, D.G., Vázquez, A.M., Nuevo, F.A., Frazin, R.A.: 2017, Comparative Study of the Three-Dimensional Thermodynamical Structure of the Inner Corona of Solar Minimum Carrington Rotations 1915 and 2081. *Solar Phys.* **292**(10), 153. DOI. <https://doi.org/10.1007/s11207-017-1179-z>.
- Mac Cormack, C., Vázquez, A.M., López Fuentes, M., Nuevo, F.A., Landi, E., Frazin, R.A.: 2017, Energy Input Flux in the Global Quiet-Sun Corona. *Astrophys. J.* **843**, 70. DOI. ADS.
- Nuevo, F.A., Huang, Z., Frazin, R., Manchester, W.B., Jin, M., Vázquez, A.M.: 2013, Evolution of the Global Temperature Structure of the Solar Corona during the Minimum between Solar Cycles 23 and 24. *Astrophys. J.* **773**(1), 9. DOI. ADS.
- Nuevo, F.A., Vázquez, A.M., Landi, E., Frazin, R.: 2015, Multimodal Differential Emission Measure in the Solar Corona. *Astrophys. J.* **811**(2), 128. DOI. ADS.
- Oran, R., Landi, E., van der Holst, B., Lepri, S.T., Vázquez, A.M., Nuevo, F.A., Frazin, R., Manchester, W., Sokolov, I., Gombosi, T.I.: 2015, A Steady-state Picture of Solar Wind Acceleration and Charge State Composition Derived from a Global Wave-driven MHD Model. *Astrophys. J.* **806**(1), 55. DOI. ADS.
- Powell, K.G., Roe, P.L., Linde, T.J., Gombosi, T.I., De Zeeuw, D.L.: 1999, A Solution-Adaptive Upwind Scheme for Ideal Magnetohydrodynamics. *Journal of Computational Physics* **154**(2), 284. DOI. ADS.
- Press, W.H., Teukolsky, S.A., Vetterling, W.T., Flannery, B.P.: 2002, *Numerical recipes in C++ : the art of scientific computing*. ADS.
- Sachdeva, N., van der Holst, B., Manchester, W.B., Tóth, G., Chen, Y., Lloveras, D.G., Vázquez, A.M., Lamy, P., Wójcik, J., Jackson, B.V., Yu, H.-S., Henney, C.J.: 2019, Validation of the Alfvén Wave Solar Atmosphere Model (AWSOM) with Observations from the Low Corona to 1 au. *Astrophys. J.* **887**(1), 83. DOI. ADS.
- Schiff, A.J., Cranmer, S.R.: 2016, Explaining Inverted-temperature Loops in the Quiet Solar Corona with Magnetohydrodynamic Wave-mode Conversion. *Astrophys. J.* **831**(1), 10. DOI. ADS.
- Serio, S., Peres, G., Vaiana, G.S., Golub, L., Rosner, R.: 1981, Closed coronal structures. II - Generalized hydrostatic model. *Astrophys. J.* **243**, 288. DOI. ADS.
- Sokolov, I.V., van der Holst, B., Oran, R., Downs, C., Roussev, I.I., Jin, M., Manchester, W.B., Evans, R.M., Gombosi, T.I.: 2013, MAGNETOHYDRODYNAMIC WAVES AND CORONAL HEATING: UNIFYING EMPIRICAL AND MHD TURBULENCE MODELS. *apj* **764**(1), 23. DOI. <https://doi.org/10.1088%2F0004-637x%2F764%2F1%2F23>.
- Spitzer, L.: 1962, *Physics of Fully Ionized Gases*. ADS.
- Tóth, G., van der Holst, B., Sokolov, I.V., De Zeeuw, D.L., Gombosi, T.I., Fang, F., Manchester, W.B., Meng, X., Najib, D., Powell, K.G., et al.: 2012, Adaptive numerical algorithms in space weather modeling. *J. Comput. Phys.* **231**(3), 870–903. DOI. <https://doi.org/10.1016/j.jcp.2011.02.006>.
- van der Holst, B.: 2019, to be accepted. *Astrophys. J.*

- van der Holst, B., Manchester, I. W. B., Frazin, R.A., Vázquez, A.M., Tóth, G., Gombosi, T.I.: 2010, A Data-driven, Two-temperature Solar Wind Model with Alfvén Waves. *Astrophys. J.* **725**(1), 1373. DOI. ADS.
- van der Holst, B., Sokolov, I.V., Meng, X., Jin, M., Manchester, I. W. B., Tóth, G., Gombosi, T.I.: 2014, Alfvén Wave Solar Model (AWSOM): Coronal Heating. *Astrophys. J.* **782**(2), 81. DOI. ADS.
- Vázquez, A.M.: 2016, Seeing the solar corona in three dimensions. *Advances in Space Research* **57**, 1286. DOI.
- Vázquez, A.M., Frazin, R.A., Kamalabadi, F.: 2009, 3D Temperatures and Densities of the Solar Corona via Multi-Spacecraft EUV Tomography: Analysis of Prominence Cavities. *Solar Phys.* **256**(1-2), 73. DOI. ADS.
- Vázquez, A.M., Frazin, R.A., Manchester, I. Ward B.: 2010, The Solar Minimum Corona from Differential Emission Measure Tomography. *Astrophys. J.* **715**(2), 1352. DOI. ADS.
- Worden, J., Harvey, J.: 2000, An Evolving Synoptic Magnetic Flux map and Implications for the Distribution of Photospheric Magnetic Flux. *Solar Phys.* **195**(2), 247. DOI. ADS.
- Wuelser, J.-P., Lemen, J.R., Tarbell, T.D., Wolfson, C.J., Cannon, J.C., Carpenter, B.A., Duncan, D.W., Gradwohl, G.S., Meyer, S.B., Moore, A.S., Navarro, R.L., Pearson, J.D., Rossi, G.R., Springer, L.A., Howard, R.A., Moses, J.D., Newmark, J.S., Delaboudiniere, J.-P., Artzner, G.E., Auchere, F., Bougnet, M., Bouyries, P., Bridou, F., Clotaire, J.-Y., Colas, G., Delmotte, F., Jerome, A., Lamare, M., Mercier, R., Mullot, M., Ravet, M.-F., Song, X., Bothmer, V., Deutsch, W.: 2004, EUVI: the STEREO-SECCHI extreme ultraviolet imager. In: Fineschi, S., Gumm, M.A. (eds.) *Telescopes and Instrumentation for Solar Astrophysics, Proc. SPIE* **5171**, 111. DOI. ADS.